The mechanical response of a magma chamber with poroviscoelastic crystal mush

Yang Liao[1], S. Adam Soule[1], Meghan Jones[1,2], Hélène Le Mével[3]

[1]Woods Hole Oceanographic Institution, Woods Hole, MA, USA
[2]Massachusetts Institute of Technology, Cambridge, MA, USA
[3]Earth and Planets Laboratory, Carnegie Institution for Science, Washington DC, USA

Key Points:

- Features of magma chamber deformation with poroviscoealstic crystal mush are examined using a mechanical model
- Coexistence of poroelastic diffusion and viscoelastic relaxation causes non-monotonous evolution in pressure, stress, and magma transport
- The evolution of magma chamber is described by two characteristic time scales depending on the material properties

Corresponding author: Yang Liao, `yliao@whoi.edu`
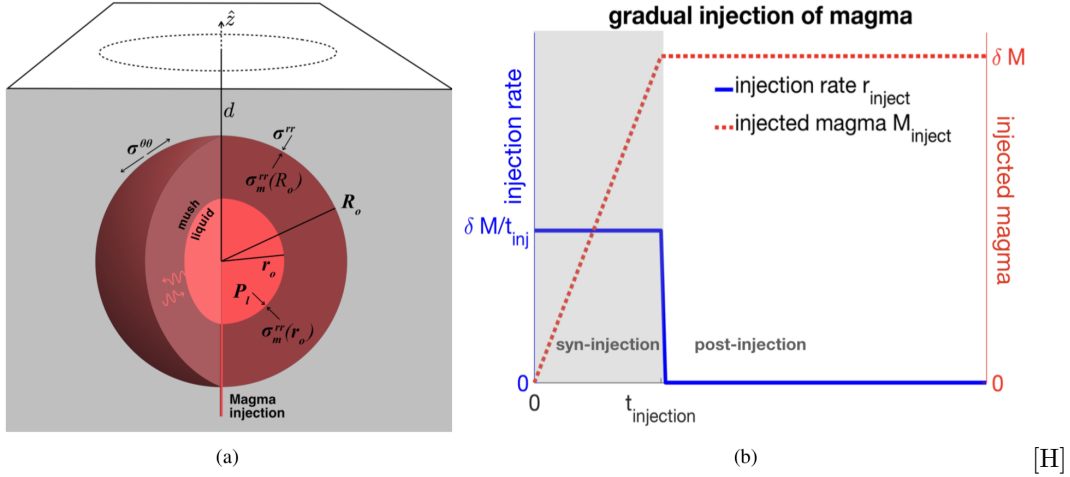
Abstract

Improved understanding of the impact of crystal mush rheology on the response of magma chambers to magmatic events is critical for better understanding crustal igneous systems with abundant crystals. In this study, we extend an earlier model by Liao et al. (2018) which considers the mechanical response of a magma chamber with poroelastic crystal mush, by including poroviscoelastic rheology of crystal mush. We find that the coexistence of the two mechanisms of poroelastic diffusion and viscoelastic relaxation causes the magma chamber to react to a magma injection event with more complex time-dependent behaviors. Specifically, we find that the system's short-term evolution is dominated by the poroelastic diffusion process, while its long-term evolution is dominated by the viscoelastic relaxation process. We identify two post-injection timescales that represent these two stages and examine their relation to the material properties of the system. We find that better constraints on the poroelastic diffusion time are more important for the potential interpretation of surface deformation using the model. We also find that the combination of the two mechanisms causes magma transport to reverse direction in the system, which would successively expose crystals to magma with different chemical compositions.

1 Background: magma chamber model with poroelastic/viscoelastic mush

Petrological studies and thermodynamic models have long indicated that crustal magmatic reservoirs (i.e., magma chambers) contain an abundance of crystal mush, where 'mush' refers to a system with melt contained in a framework of crystals (Cashman et al., 2017). In recent decades, many research efforts have been devoted to understanding how crystal mush evolves and interacts with magma, using principles in thermodynamics, geochemistry, and geophysics. These models demonstrate the importance of crystal mush in a magma chamber's thermal and chemical evolution, as well as in some physical processes such as the segregation of a liquid phase (Sparks & Cashman, 2017; Bachmann & Huber, 2016; Singer et al., 2018; McKenzie, 2011, e.g.,). However, fewer studies have evaluated the impact of crystal mush on magma chamber deformation, pressurization, stress evolution in the host rocks and surface deformation (Gudmundsson, 2012; Liao et al., 2018). Liao et al. (2018) demonstrated that crystal mush can significantly alter the response of a mushy chamber to magma injection events relative to the conventional mush-less, fluid-filled chamber. The model examined two possible rheologies of crystal mush, poroelasticity and viscoelasticity, which are two end members of a more general rheology of poroviscoelasticity. Liao et al. (2018) showed that poroelasticity and viscoelasticity cause similar features in the magma chamber's post-injection evolution (e.g., post-injection pressure decrease and stress increase), but did not examine how the chamber behaves when poroelastic and viscoelastic mechanisms coexist. Here, we expand on the poroelastic/viscoelastic model in Liao et al. (2018) to explore the effects of poroviscoelastic mush on the response of a magma chamber to a magma injection event and the resulting ground deformation.

2 Magma chamber model with poroviscoelastic mush in a half-space

For ease of comparison with previous mechanical magma chamber studies (Dragoni & Magnanensi, 1989; Karlstrom et al., 2010; McTigue, 1987; Segall, 2016; Liao et al., 2018, e.g.,), we adopt the same spherical geometry of the poroelastic chamber model as Liao et al. (2018) shown in Figure 1a. The magma chamber consists of a three-dimensional spherical core of liquid magma within a shell of poroviscoelastic mush with pre-injection porosity ϕ_o. The magma chamber is hosted in a half space of linear elastic crust with a traction-free upper surface. We approximate the surface deformation in vertical and

Figure 1. (a) Geometry of the mushy magma chamber model (adapted from (Liao et al., 2018)), with several important quantities marked including: core pressure P_l, pore pressure P_f, tensile stress $\sigma^{\theta\theta}$, force balance on the two interfaces, and transport of magma in the mush region (red curved arrows). The chamber is at depth d from a free surface with radius R_o and liquid core radius r_o. (b)Accumulated amount of injected magma M_{inject} (y axis on the right) and injection rate r_{inject} (y axis on the left) as functions of time, t_{inj} is the length of the injection. The shaded area indicates the syn-injection period $0 \leq t \leq t_{inj}$.

horizontal directions following the same approach used in earlier studies (Segall, 2016, 2019; McTigue, 1987).

We assume a simplified magma injection event, where magma enters into the liquid core at a constant injection rate during the injection period $0 \leq t \leq t_{inj}$ (Figure 1b), leading to the accumulated mass of injected magma $M_{inject} = \frac{t\delta M}{t_{inj}}$ for $t \leq t_{inj}$ and $M_{inject} = \delta M$ for $t > t_{inj}$.

During and after the injection, magma is allowed to flow across the liquid-mush interface and within the mush, driven by the gradient of pore pressure P_f. The motion of pore magma follows Darcy's law and mass conservation

$$\vec{q} = -\frac{\kappa}{\eta_f}\nabla P_f \tag{1a}$$

$$\frac{\partial m}{\partial t} + \nabla \cdot (\rho_f \vec{q}) = 0 \tag{1b}$$

where $\vec{q}$ is the Darcy velocity (positive values indicates the flow direction from magma core to the chamber wall), κ is the permeability of the mush, η_f is the magma viscosity, and ρ_f is the density of pore magma. The variation in fluid content is described by the function $m(r,t)$, which is defined as the change in pore fluid mass per un-deformed volume of mush located at radius r (positive value $m > 0$ indicates that the pores in the mush gain magma). The integration of m across the mush shell leads to the total amount of magma transported between the liquid and the mushy region

$$M_{leak} = \int_{r_o}^{R_o} 4\pi r^2 m(r,t)\mathrm{d}r \tag{2}$$

where $M_{leak}(t)$ is the accumulated amount of magma transported across the magma-mush boundary. $M_{leak} > 0$ indicates that magma is flowing from the liquid core to the mushy shell (i.e., 'leaking'). We calculate the pressure change P_l in the liquid core upon mass injection assuming isothermal compression, which depends on the amount of injected magma M_{inject}, the amount of magma exchanged between the core and mush M_{leak}, and the volume change of the liquid core indicated by the radial displacement $u_m(r_o)$ on the core-mush interface. After linearization, the pressure change is (Liao et al., 2018):

$$P_l(t) = K_l(\frac{M_{inj}(t)}{M_o} - \frac{M_{leak}(t)}{M_o})\left(1 - 3\frac{u_m(r_o, t)}{r_o}\right) \tag{3}$$

where K_l is the bulk modulus (1/compressibility) of the core and injected magma, and M_o is the pre-injection magma mass in the liquid core (see Appendix A). The injection causes the chamber to inflate, which leads to increased displacement $\vec{u}_{rock}$ and elastic stress $\boldsymbol{\sigma}_{rock}$ in the surrounding crustal rocks, following the constitutive relation for linear elastic material

$$\boldsymbol{\sigma_{rock}} = (K_r - \frac{2}{3}\mu_r)\nabla \cdot \vec{u}_{rock}\boldsymbol{I} + \mu_r\left(\nabla\vec{u}_{rock} + \nabla\vec{u}_{rock}^T\right) \tag{4}$$

where K_r and μ_r are the bulk and shear modulus of the host rock, respectively. It is worth noting that both the stress component in the tensile direction $\sigma^{\theta\theta}$ on the chamber-rock boundary (Figure 1a) and overpressure increase during the inflation of the chamber, which may cause the chamber's wall to rupture (Pinel & Jaupart, 2003; Grosfils, 2007; Currenti & Williams, 2014; Albino et al., 2010; Karlstrom et al., 2010; Gudmundsson, 2012; Zhan & Gregg, 2019, e.g.,). In our current model, the rupture of magma chamber is omitted. We describe the deformation and stress in the crystal mush using a poroviscoelastic rheology, combining linear poroelasticity with a Maxwell viscoelastic model. The strain $\boldsymbol{\epsilon}_m$, stress $\boldsymbol{\sigma}_m$, variation in fluid content m and pore pressure P_f obey the constitutive relations

$$\left(\frac{\partial\boldsymbol{\sigma}_m}{\partial t} + \frac{\mu_m}{\eta_m}\boldsymbol{\sigma}_m\right) - \frac{1}{3}\frac{\mu_m}{\eta_m}Tr(\boldsymbol{\sigma}_m)\mathrm{I} = 2\mu_m\frac{\partial\boldsymbol{\epsilon}_m}{\partial t} + \left(K_m - \frac{2}{3}\mu_m\right)\frac{\partial Tr(\boldsymbol{\epsilon}_m)}{\partial t}\mathrm{I} - \alpha\frac{\partial P_f}{\partial t}\mathrm{I} \tag{5a}$$

$$m = \rho_f\alpha\left(Tr(\boldsymbol{\epsilon}_m) + \frac{\alpha}{K_u - K_m}P_f\right) \tag{5b}$$

where K_m is the bulk modulus of the crystalline framework (i.e., drained modulus), and K_u is the bulk modulus of the crystal-fluid ensemble (i.e., undrained modulus). α is the poroelastic constant (also known as Biot constant) with a value from 0 to 1, determined by the strength of the crystalline framework relative to that of the single crystal (represented by its bulk modulus K_s) as $\alpha = 1 - \frac{K_m}{K_s}$. We assume that the crystalline network itself is weak compared to the single crystals, thus $K_m << K_s$, leading to a large α. We use $\alpha = 0.9$ for the rest of the study. The viscoelastic relaxation of the crystalline matrix is determined by its rigidity μ_m and viscosity η_m. We can verify that the poroelastic and viscoelastic rheologies are two end members of the poroviscoelastic rheology: when matrix viscosity $\eta_m \to \infty$, (5) reduces to linear poroelasticity (Cheng, 2016); when pore pressure is decoupled from the stress (i.e., $\alpha = 0$), (5) becomes the classical Maxwell formulation (Segall, 2016; Jellinek & DePaolo, 2003). In the model, we assume that the viscous relaxation of the mush network primarily occurs in the shear component, hence omitting the compaction effect. The deformation in the host rocks and the mush shell obey quasi-equilibrium condition

$$\nabla \cdot \boldsymbol{\sigma}_{m,rock} = 0 \tag{6}$$

and boundary conditions,

$$P_l + \sigma_m^{rr}(r_o) = 0 \tag{7a}$$

$$P_l - P_f(r_o) = 0 \tag{7b}$$

$$\sigma_m^{rr}(R_o) - \sigma_{rock}^{rr}(R_o) = 0 \tag{7c}$$

$$\vec{u}_m(R_o) - \vec{u}_{rock}(R_o) = 0 \tag{7d}$$

$$\frac{\partial P_f}{\partial r}(R_o) = 0 \tag{7e}$$

$$u_{rock}(r \to \infty) = 0 \tag{7f}$$

which prescribes force balance, continuity (in displacement and fluid pressure) at both the magma-mush and mush-rock boundaries, and a chamber wall impermeable to the pore magma. The above constraints determine the unique time-dependent solutions, which are calculated using Laplace transform (see Appendix A). We follow earlier studies to approximate the surface deformation resulting from the deformation of a spherical chamber (McTigue, 1987; Segall, 2016, 2019)

$$
\begin{aligned}
u_z(\rho, t) &= -\frac{\sigma_m^{rr}(R_0, t)}{\mu_r} \frac{R_0^3}{d^2} \frac{1-\nu}{\left(\frac{\rho^2}{d^2}+1\right)^{\frac{3}{2}}} \\
u_\rho(\rho, t) &= -\frac{\sigma_m^{rr}(R_0, t)}{\mu_r} \frac{R_0^3}{d^2} \frac{1-\nu}{\left(\frac{\rho^2}{d^2}+1\right)^{\frac{3}{2}}} \frac{\rho}{d}
\end{aligned}
\tag{8}
$$

where u_z and u_ρ are the vertical and horizontal displacement on the surface $z = 0$, measured at a radial distance ρ; ν is the Poisson's ratio of the elastic crust, σ_m^{rr} is the radial component of stress at the chamber-crust interface. Earlier works demonstrated that when the depth of the magma chamber d is modestly larger than the chamber's radius $d/R_0 \geq 2$, (8) provides good estimations for the deformation on the surface (Segall, 2016). In our study, we assume d/R_0 between 3 to 10 for precise approximation of the ground deformation. Because the poroviscoelastic mush is subjected to two different mechanisms (poroelastic diffusion and viscoelastic relaxation), we identify two timescales that represent the two mechanisms respectively (see Appendix A)

$$\tau_{diffusion} = \frac{R_o^2 \eta_f}{\kappa} \frac{\alpha^2 \left(K_u + \frac{4}{3}\mu_m\right)}{(K_u - K_m)\left(K_m + \frac{4}{3}\mu_m\right)} \tag{9a}$$

$$\tau_{relaxation} = \frac{\eta_m}{\mu_m} \tag{9b}$$

where $\tau_{diffusion}$ is the poroelastic diffusion time and $\tau_{relaxation}$ is the viscoelastic relaxation time. We verify that the crystal mush is poroelastic when $\tau_{relaxation} = \infty$, and viscoelastic if $\tau_{diffusion} = \infty$. Given the uncertainties in parameters such as mush permeability, crystalline rigidity and viscosity, magma viscosity and compressibility, $\tau_{relaxation}$ and $\tau_{diffusion}$ can have a wide range of values. For example, the poroelastic diffusion time $\tau_{diffusion}$ ranges from 6 days to 160 years assuming a magma chamber with 1km radius and parameters similar to those used in Liao et al. (2018) and others ($\alpha = 0.9$, $\mu_m^o = 1$ GPa, $K_f = 1$ GPa, $\kappa \in [10^{-10}, 10^{-8}]m^2$, and $\eta_f \in [10^1, 10^3]$ Pa.s). Further, assuming a crystalline viscosity similar or smaller than heated rock ($\eta_m \in [10^{16}, 10^{18}]$ Pa.s), the resulting viscoelastic relaxation time $\tau_{relaxation}$ ranges from 4 months to 30 years (Segall, 2016; Cheadle et al., 2004; McKenzie, 2011). Below, we choose the case of a poroviscoelastic mush subjected to both mechanisms with comparable time scales $\tau_{diffusion} = \tau_{relaxation}$ to illustrate the basic features of a poroviscoelastic mushy chamber.

It is worth noting that, although the current model fills the gap in rheology assumed in Liao et al. (2018), many assumptions are still made to simplify the problem. These

assumptions, including the spherical geometry, radial symmetry in magma chamber deformation, homogeneity in crystal mush distribution, and neglected thermal effects could all affect how a more realistic mushy magma chamber reacts to magma injection, and, while beyond the scope of this study, should be examined and evaluated in future studies.
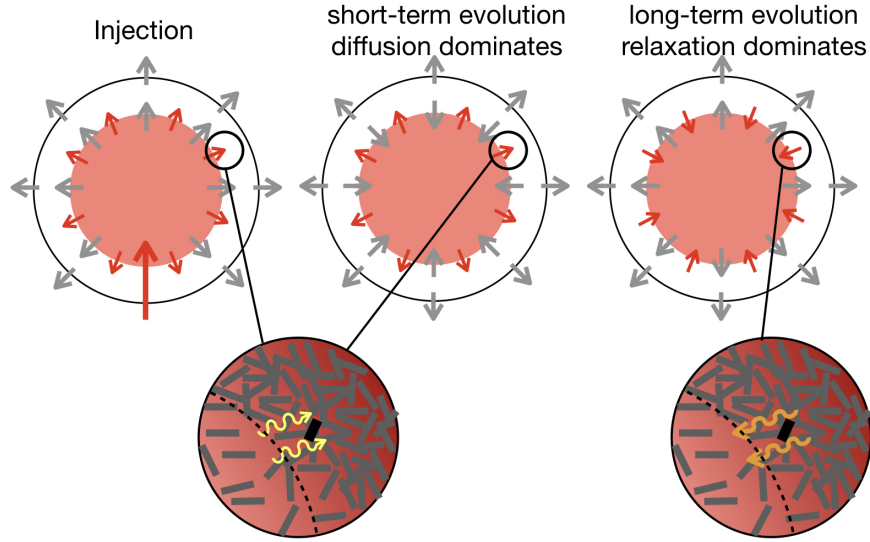
3 Model results

Similar to poroelastic or viscoelastic mush, the poroviscoelastic mush causes the magma chamber and its surrounding crust to continue evolving after the injection has stopped, as opposed to a fluid chamber that reaches steady state as soon as the injection ends (Figure 4). We find that the time-dependent evolution of the poroviscoelastic mushy chamber is, at different times, dominated by either poroelastic diffusion or viscoelastic relaxation. Below, we examine the features of deformation, pressure, stress, and magma transport in both stages.

3.1 Syn- and post- injection evolution of magma chamber with poroviscoelastic mush shell

We examine time-dependent magma chamber deformation during three stages: syn-injection, shortly after the injection, and long the after the injection. During the syn-injection period, magma is added into the liquid core at a constant rate (shaded area in Figure 1b), increasing the pressure in the core magma (Figure 4a), and pushing both the magma-mush boundary at $r = r_o$ and the mush-rock boundary at $r = R_o$ outward (Figure 3a). The expansion of the whole chamber causes the tensile stress in the rock surrounding the chamber and ground deformation to increase with time (Figure 4b, c). During the syn-injection period, pressure in the liquid core always exceeds the pore pressure in the mush shell. As a result, some magma in the liquid core flows into the mush (Figure 5a), increasing the pore pressure in the mush (See Figure B2 in Appendix B). The syn-injection period ends at $t = t_{inj}$, when the injection rate drops to 0. At the end of the injection, a fluid pressure gradient remains that sustains magma flow from the core fluid into the mush.
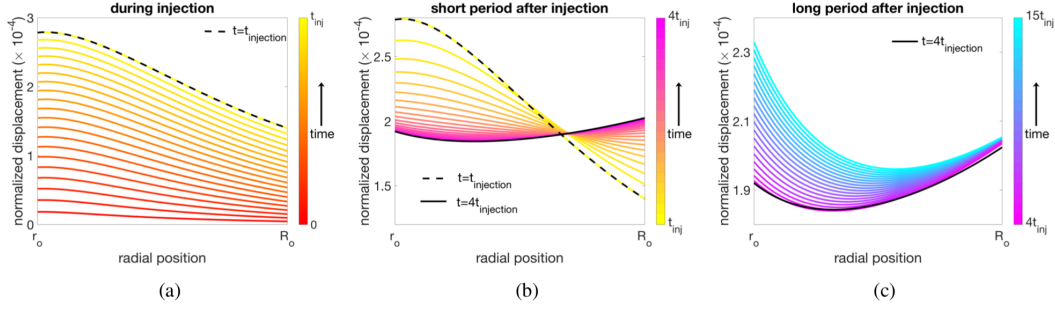
The short post-injection period begins when the injection stops, at $t = t_{inj}$. During this period, the evolution of the deformation is similar to that of a chamber with poroelastic mush (see Figure 3b in Liao et al. (2018)). Without more magma injection, the fluid core loses magma due to porous flow into the mush, causing the pressure in the liquid core to decrease. The liquid-mush boundary retracts inward and the liquid core shrinks in response to the decreasing core pressure and mush expansion (Figure 5b, Figure 4a, Figure 3b). Although viscous relaxation also occurs during this period, it is not strong enough to noticeably deviate the evolution of the system from that of a poroelastic chamber. Because of these qualitative similarities, we consider the short time period post-injection evolution to be dominated by the poroelastic diffusion mechanism (middle panel in Figure 2).

With time, the effect of viscoelastic relaxation becomes more apparent – as the poroelastic effects diminish – and the system begins to show features similar to those displayed by a purely viscoelastic mushy chamber. During this period, the viscoelastic relaxation causes outward creeping and compression of the whole mush shell (Figure 3c), reversing the motion of the previously retracting liquid-mush boundary and pushing it outward again (Figure 2b). The outward movement of the liquid-mush boundary causes the volume of the liquid core to expand, and the pressure in it to further decrease (Figure 4a). The outward creeping of the mush-rock boundary causes the tensile stress in the host rock and ground deformation to continue increasing (Figure 4b, Figure 8a). Eventually, the liquid core pressure becomes less than the pore pressure in the adjacent mush due to the loss of core magma and the expansion of the core. This reverses the pressure gra-

Figure 2. Cartoon illustration of the three stages in the dynamic evolution of a mushy magma chamber: syn-injection stage, poroelastic diffusion-dominated stage, and viscoelastic relaxation-dominated stage. Grey arrows indicate the direction of the radial displacement of the magma-mush and mush-rock boundaries, and red arrows show the direction of magma transport. Illustration of pore magma transport and their possible chemical signatures are shown in the zoom-in panels. The deformation dominated by poroelastic diffusion is consistent with the evolution shown in Figure 3(b), and the viscous relaxation-dominated regime is consistent with Figure 3(c).
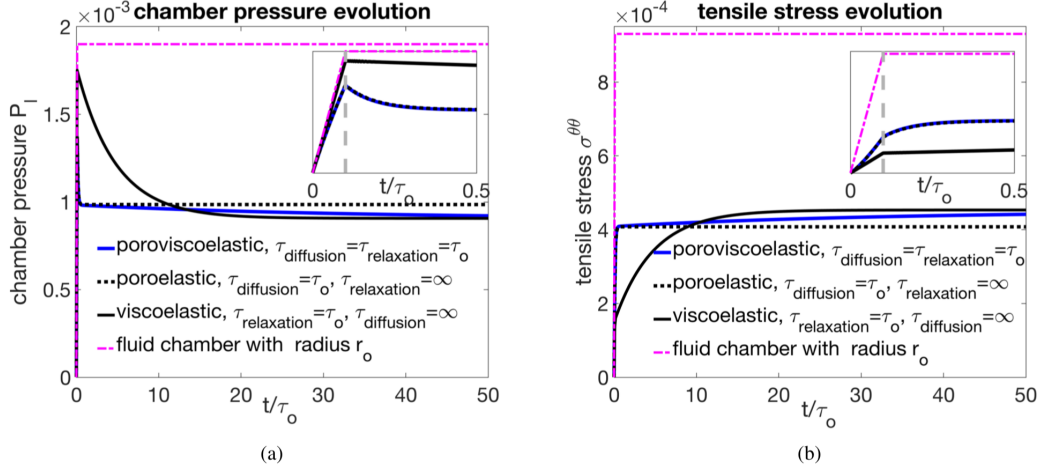
Figure 3. Displacement in the poroviscoelastic mush shell during and after injection. The thickness of the mush shell is half of the total chamber radius ($r_o = R_o/2$) with equal relaxation and diffusion times $\tau_{relaxation} = \tau_{diffusion}$. A total amount of magma $\delta M = 0.02 M_o$ is injected for the duration of $t_{injection} = \tau_{diffusion}/10$. Left panel shows the displacement $u(r)/R_o$ (normalized by the chamber radius) as a function of radial position r during the injection $0 \leq t \leq t_{injection}$, where the black dash line indicates the displacement profile at the end of the injection $t = t_{injection}$; middle panel shows the displacement during a short time period after the injection $t_{injection} \leq t \leq 4t_{injection}$, where the black dash line and black solid line show the profile at $t = t_{injection}$ and $t = 4t_{injection}$, respectively; right panel shows the displacement for longer period after the injection $t > 4t_{injection}$, where the black solid line indicates the profile at $t = 4t_{injection}$. The left and middle panels are qualitatively similar to the evolution of a poroelastic shell (see Figure 3 in Liao et al. (2018)). The poroelastic dominated and viscoelastic dominated deformations are also shown in cartoon illustration in Figure 2. Other parameters include $\alpha = 0.9, r_o/R_o = 1/2, K_f/\mu_r = 0.5, K_l/\mu_r = 0.1, K_s/\mu_r = 5/3, \mu_m/\mu_r = 1/2, \phi_o = 0.2$.

dient direction at the magma-mush boundary resulting in porous flow from the mush into the core (Figure 5c), returning most of the previously leaked magma back into the core at a slower speed (Figure 6). This stage, where the magma chamber is dominated by viscoelastic relaxation, lasts until the system reaches a new steady state. Although the decrease in chamber pressure and increase in tensile stress of the crust during this period are similar in sign to the poroelastic diffusion dominated stage, the rate of change in these quantities is much lower, as is reflected by a nearly indiscernible strain rate at the wall of the chamber (Figure B1 in Appendix Appendix B) and slow increase in ground elevation (Figure 8).

3.2 Timescales in post-injection evolution

Compared to the poroelastic case where one timescale can be identified to describe its post-injection evolution (Liao et al., 2018), a chamber with poroviscoealstic mush requires two timescales to characterize the non-monotonic changes in pressure, stress, and magma transport (Figure 4 and 6). To determine the short-period evolution time t_{post}^{short}, we numerically calculate the time it takes for the pressure gradient at the magma-mush interface to reverse, and for magma to begin to leak back into the liquid core (Figure 6b) after a sudden injection. To determine the long-period evolution time t_{post}^{long}, we calculate the time it takes for the system to approach a final steady state after injection, using the same analytical approach in Liao et al. (2018) for a poroelastic/viscoelastic chamber. Following a sudden injection at $t = 0$, the evolution of the system during time period $0 < t \leq t_{post}^{short}$ is consistent with a poroelastic diffusion dominated stage, represented by a relatively rapid decrease in chamber's pressure P_l, a rapid increase in tensile stress $\sigma^{\theta\theta}$, and core-to-mush magma transport. Over the time period $t_{post}^{short} < t \leq$
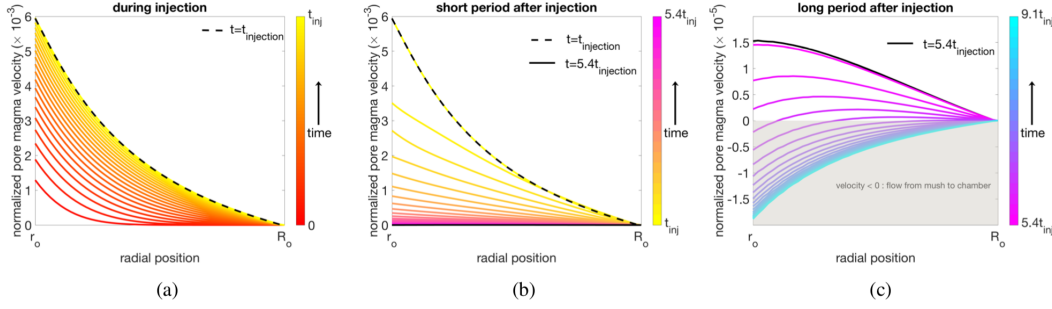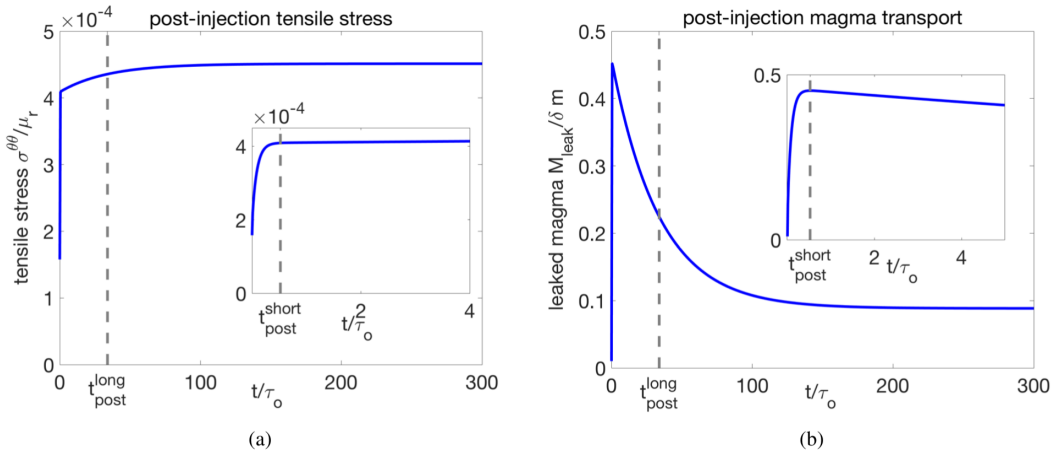
Figure 4. Syn- and post-injection evolution of liquid core fluid pressure P_l (panel a), and tensile stress $\sigma^{\theta\theta}$ (panel b) as functions of time, with initial short period evolutions zoomed in insert panels. Purple broken line corresponds to a mushless liquid chamber with the mushy chamber's liquid core radius $r_0 = 0.5R_0$; blue solid lines, black dotted lines, and black solid lines correspond to a mushy chamber with poroviscoelastic, poroelastic, or viscoelastic mush shell respectively. Other parameters are the same as in Figure 3.

t_{post}^{long}, the system behaves consistently with a viscoelastic relaxation dominated stage, characterized by a slower decrease in chamber's pressure, slow increase in tensile stress, and mush-to-core magma transport. Over the time period $t > t_{post}^{long}$, the system remains dominated by viscoelastic relaxation, although its evolution is slow enough to be regarded as approaching a new steady state.
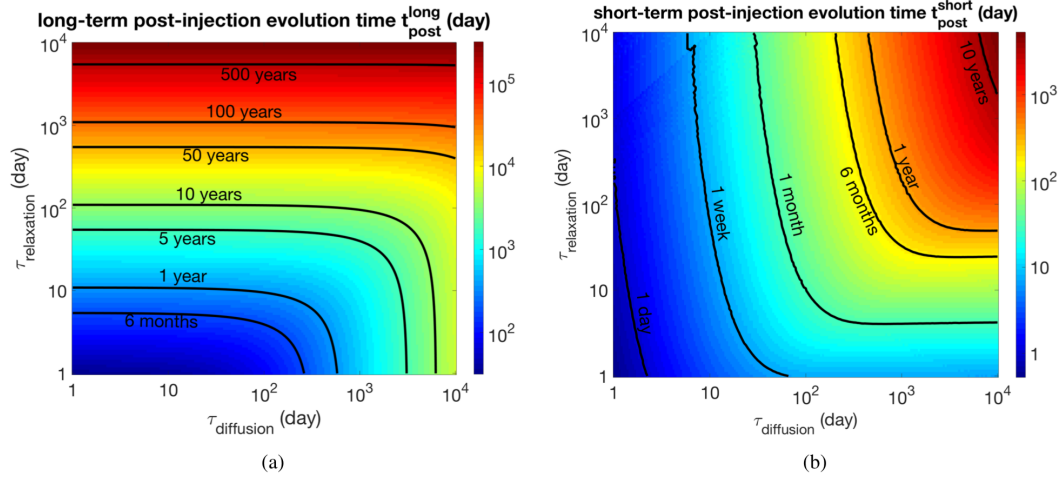
We found that both t_{post}^{short} and t_{post}^{long} depend on the material properties (e.g., $\tau_{diffusion}$ and $\tau_{relaxation}$) and geometry of the system (e.g., r_o/R_o). Although $\tau_{diffusion}$ and $\tau_{relaxation}$ both affect t_{post}^{short} and t_{post}^{long}, it is clear that the short-period evolution time t_{post}^{short} is more sensitive to $\tau_{diffusion}$; whereas the long-period evolution time t_{post}^{long} changes more sensitively with $\tau_{relaxation}$(Figure 7). Considering that the early post-injection evolution of the system corresponds to faster change and higher strain-rate, we consider it to be potentially more relevant to geophysical observations (e.g., deformation, seismicity), hence constraining the value of $\tau_{diffusion}$ is important for comparing the model to field data. According to (9a), $\tau_{diffusion}$ is determined by parameters with potentially large degrees of uncertainty, such as the poorly constrained mush permeability κ, and the magma viscosity η_f, which has a wide range of values depending on temperature, degree of crystallization, and chemical compositions. Reasonable variations in these parameters can cause $\tau_{diffusion}$ to vary across orders of magnitudes from days to hundreds of years. For these reasons, better constraints on these parameters via petrological observations and thermodynamic models are crucial for evaluating rheological models such as the one proposed here. It is also worth noting that the two post-injection timescales are defined based on the evolution of magma chamber following a sudden injection, and can qualitatively describe the behavior of a mushy chamber when the injection is much shorter than both $\tau_{diffusion}$ or $\tau_{relaxation}$. For very long injection times (i.e., low injection rates), however, the diffusion-dominated stage becomes very short, and the chamber would qualitatively display characteristics of the relaxation-dominated stage soon after the injection (see Figure B3 in Appendix Appendix B).

(a) (b) (c)

Figure 5. Darcy velocity of pore magma $\vec{q}$ (radial component) in the poroviscoelastic mush shell, as a function of radial position r, during and after injection. The thickness of the mush shell is half of the total chamber radius ($r_o = R_o/2$) with equal relaxation and diffusion time $\tau_{relaxation} = \tau_{diffusion}$. A total amount of magma $\delta M = 0.02 M_o$ is injected for the duration of $t_{injection} = \tau_{diffusion}/10$. The velocity is normalized by velocity scale $\kappa \mu_r / \eta_f R_o$, where κ is the mush permeability, μ_r is the crustal rock rigidity, η_f is the viscosity of pore magma, and R_o the radius of the chamber. Positive values of q indicate the magma flowing from the core to the mush, and negative values indicate flow from the mush into the core. Left panel corresponds to syn-injection evolution $0 \leq t \leq t_{injection}$, where the black dash line indicates the velocity profile at the end of the injection $t = t_{injection}$; middle panel shows the pore magma velocity during a short time period after the injection $t_{injection} \leq t \leq 5.4t_{injection}$, where the black dash line and black solid line show the profile at $t = t_{injection}$ and $t = 5.4t_{injection}$, respectively; right panel shows the velocity for longer period after the injection $t > 5.4t_{injection}$, where the black solid line indicates the profile at $t = 5.4t_{injection}$. The poroelastic dominated and viscoelastic dominated pore magma flow direction are also shown in cartoon illustration in Figure 2. The region where $q < 0$ in the right panel indicates the change in flow direction of the pore magma, which corresponds to the onset of decrease in the amount of cumulated leaked magma (see Figure B2 in Appendix B for the amount of transported magma). Other parameters are the same as in Figure 3.

(a) (b)

Figure 6. Post-injection short-term (insert panels) and long-term evolution of tensile stress (left) and leaked magma M_{leak} (right) from the liquid core to the shell following a sudden injection. Grey dashed lines indicate the two post-injection timescales t_{post}^{long} and t_{post}^{short} identified for the post-injection evolution.
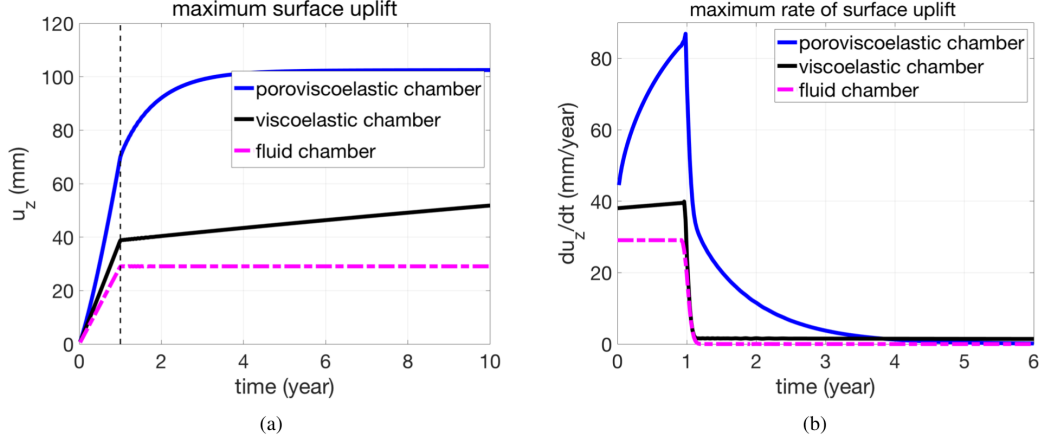
Figure 7. Post-injection short-term evolution timescale t_{post}^{short} (right) and long-term evolution timescale t_{post}^{long} (left) shown as functions of viscoelastic relaxation time $\tau_{relaxation}$ and poroelastic diffusion time $\tau_{diffusion}$. The long-term evolution time t_{post}^{long} is more sensitive to the change in viscoelastic relaxation time; the short-term evolution time is more sensitive to the change in poroelastic diffusion time.

4 Implications and future studies

Our model allows to explore the consequences of magma injection in a chamber with a poroviscoelastic mush layer on some common observations made in magmatic systems. In this section we discuss two examples of implications of our model for geodesy and petrology. Although these predictions are highly generalized at this stage, they indicate the potential for future model development that incorporates more realistic and complex features of natural magmatic systems to provide novel ways to interpret volcano geophysical and petrological data.

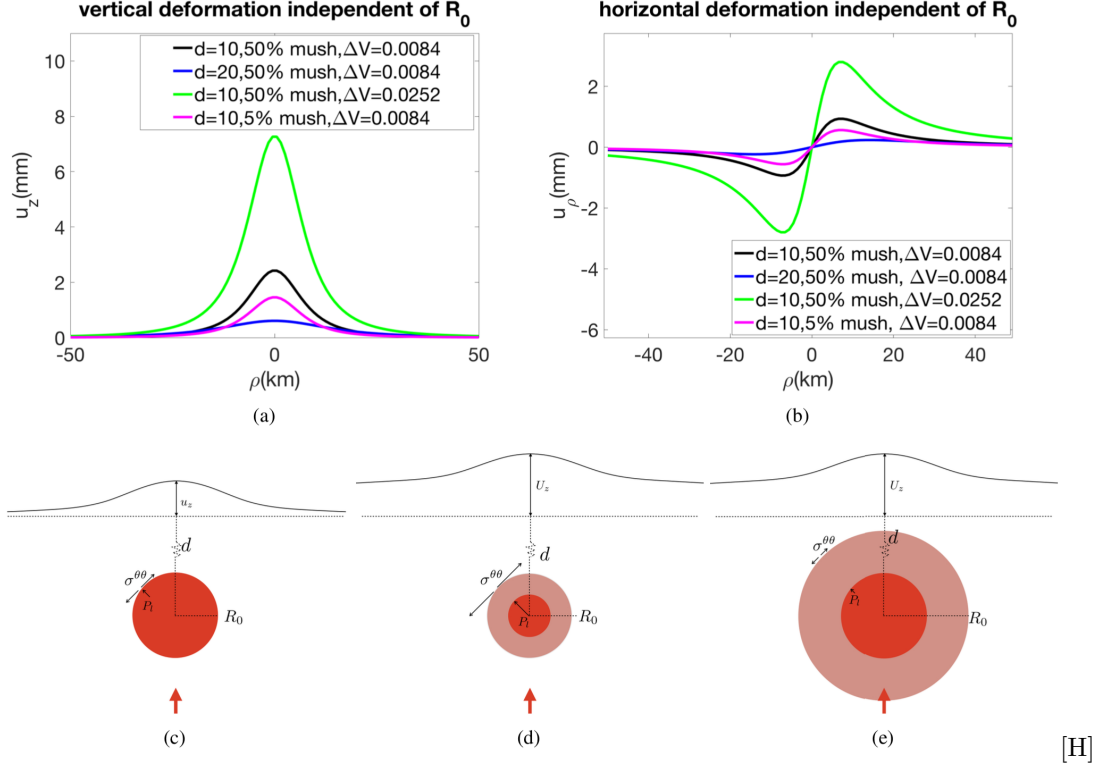### 4.1 Implication on the interpretation of ground deformation

One consequence of the existence of mush in a magma chamber is prolonged ground deformation after the injection has ceased due to redistribution of pore magma and/or relaxation of the crystalline framework. For example, a 1.5 km magma chamber at 4.5 km depth undergoing a one-year injection with a moderate rate of $1.12 m^3/s$ would experience an additional 30mm of ground uplift (1/3 of total uplift), in the period of three years after the injection has stopped (Figure 8a). For an injection at a constant rate, a mushy chamber results in time-dependent changes in the rate of ground deformation distinct from a liquid chamber hosted in elastic rock. Specifically, our mushy chamber model predicts an increasing syn-injection ground uplift rate, and decreasing post-injection uplift rate, such that the strain rate and uplift rate reach their maximum at the end of the injection (Figure 8b). These characteristics (i.e., increasing then decreasing uplift rates of ground deformation) have been observed at various volcanic systems, for example, at Long Valley Caldera, Campi Flegrei, and Laguna del Maule (Le Mével et al., 2015). At Laguna del Maule volcanic field in Chile, they are explained as consequences of time-varying injection rates (Le Mével et al., 2016). While time-dependent injection rates driven by magma supply dynamics from deeper reservoirs or mantle plumes are possible (Poland et al., 2012; Bato et al., 2018, e.g.), the combination of injection, pore magma transport, and relaxation in a mushy chamber provides an alternative explanation that corresponds to many physical models which still typically consider injection rates to be constant or

Figure 8. Vertical surface uplift (panel a) and rate of surface uplift (panel b) as functions of time during and after injection, for a liquid chamber (purple broken lines) and a mushy chamber with either poroviscoelastic (blue solid lines) or viscoelastic (black solid lines) mush (diffusion and/or relaxation time $\sim$ 10 years). The center of the magma chamber is located at a depth of 4.5km, with a radius of 1.5km. The injection assumes a volumetric injection rate of $1.12m^3/s$ for the duration of 1 year, indicated by black dash line in panel a. The rate of ground deformation has been smoothed using a piece-wise, low-pass Butterworth filter to eliminate numerical artifacts caused by the Laplace inversion algorithm.

decrease exponentially (Segall, 2016; Huppert & Woods, 2002; Biggs & Pritchard, 2017). The mushy chamber model provides an alternative explanation for such features, where the combination of injection, pore magma transport and relaxation modulate deformation rates.

Although the time-dependent features in ground deformation may suggest the existence of a mushy chamber, the magnitude of ground deformation caused by a deforming mushy chamber is limited in its ability to constrain key parameters of the chamber such as its volume, pressure, and likelihood to rupture. Similar to classical models, the depth of the magma chamber d can be straightforwardly obtained from (8) by comparing the vertical and horizontal components of the displacement $d = u_z \rho / u_\rho$ (Segall, 2019). With d and the elastic properties of crustal rock constrained, the ground deformation further constrains $\sigma_m^{rr} V_0 \propto \Delta V$ (or $P_l V_0$ if there is no mush, ΔV is injected volume), but can not constrain pressure/stress and chamber volume individually. We find that when the depth d is fixed, the amplitude of ground deformation $u_{\rho,z} \propto \Delta V \frac{R_o^3}{r_o^3}$. Therefore the ground deformation increases with the volume ratio of mush and is independent of the size of the chamber (Figure 9): for the same injection event, a large chamber with 50% mush and a small chamber with 50% mush cause the same ground deformation, and that a liquid chamber always causes smaller ground deformation than a mushy chamber, regardless of its size. On the other hand, the pressure and tensile stress depend on both the volume ratio of mush and the total volume of the chamber. Therefore, a small liquid chamber may cause smaller ground elevation compared to a large mushy chamber, but is more likely to erupt due to higher pressure and tensile stress. This non-uniqueness poses a challenge to applying our forward models to interpret ground deformation data. Combining ground deformation data with other geophysical measurements, such as seismic, electromagnetic, and gravimetry measurements, is necessary to provide constraints on the volumes of liquid and mush, and to increase the applicability of models as proposed here (Magee et al., 2018; Ward et al., 2014).

Figure 9. (a) and (b) show vertical and horizontal displacement at the surface for different combination of burial depth d (km), mush volume fraction, and injected volume ΔV (km^3). The ground deformation increases with mush volume fraction, injected volume ΔV, and decreases with burial depth d, but does not vary with the size of the chamber. (c)-(e) are cartoons illustrating three different magma chambers under the same magma injection. Tensile stress, chamber pressure, and ground deformation in the new steady state ($t \rightarrow \infty$) are shown in all three cases (not to scale). Case (c) represents a liquid chamber with radius r_0; case (d) represents a mushy chamber with total chamber radius r_0; case (e) represents a mushy chamber with liquid core radius r_0. All three chambers are buried at the same depth d and subjected to the same amount of injected magma ΔV. Cases (d) and (e) cause the same ground deformation as they have the same mush volume fraction, but cause different tensile stress and pressure.

4.2 Implication on the interpretation of crystal zoning

One implication of the poroviscoelastic magma chamber model for petrologic interpretations is the potential reversal of melt transport directions to produce chemical zonation in phenocrysts via exposing crystals to pore magma with evolving chemical fingerprints (Figure 2, Figure 6b and Figure B2). Chemically zoned phenocrysts are seen as sensitive recorders of magmatic conditions. A variety of processes are linked to zonation including changes in the temperature, composition, pressure, water content, and oxygen fugacity of the host magma (Ruprecht & Wörner, 2007, e.g.,) or by transport of crystals through gradients in physico-chemical properties in a zoned magma chamber (Ginibre et al., 2002, e.g.,). Whereas simple zonation of a mafic core and more evolved rim (or vice versa) are commonly explained by magma mixing events; more complex zonation, including oscillatory zoning, require similarly complex physical mechanisms ((Perugini et al., 2005; Ginibre & Wörner, 2007, e.g.,)). An example from the 2001 eruption of Shiveluch Volcano finds multiple phases with distinct zoning features ((Humphreys et al., 2006)). Sieve textured Ab-rich plagioclase feldspars with overgrowths of An-rich rims are interpreted to reflect the mixing of a hotter, more primitive melt with the existing evolved melt. In the same eruption, oscillatory zoned plagioclase are observed that are interpreted to reflect oscillations in pressure and pH2O resulting from unstable conduit flow during ascent. A subset of oscillatory zoned plagioclase have patchy cores that are typically more anorthitic and are thought to form from a more primitive melt than simple oscillatory zoned phenocrysts.

These interpretations of distinct mechanisms for zoning are well-supported and another explanation is not necessarily required; however, we postulate that similar zonation features could develop in phenocrysts due to transport of melt in and out of the mush zone. Oscillatory zoning, for example, could form near the melt-mush interface as crystals are washed by outward (e.g., more primitive, hotter) and inward (e.g., less primitive, cooler) melt. Sieve textured phenocrysts might be located further into the mush zone, where only a larger injection event would allow a more primitive melt to encounter the crystals, and which would be less subjected to significant changes in flow direction. In addition to injection-induced pressure gradients, other processes such as vesiculation and or gas loss may also allow melt transport through the mush producing 'in-place'zonation. The potential to produce chemical zonation within magmatic mush merits further examination including the physical processes of disaggregating the mush and the probability of incorporating those crystals into the melt (Parmigiani et al., 2014, e.g.,), and the examination of asymmetric zonation patterns (e.g., non-concentric) that might result in a partially interconnected network of crystals.

4.3 Future studies

Our current viscoelastic model serves as a foundation for understanding of how mush rheology impacts the first-order mechanical responses of a magmatic reservoir, with assumed simplifications such as isothermal condition, radial symmetry, uniform material properties, and simplified injection time series. As natural volcanic system are more complex, there is room for future refinement of the current model. Theses future studies will yield a more thorough understandings of the role of crystal mush in magmatic reservoirs with more complex features or under more realistic conditions, such as non-uniform (e.g., radially varying) material properties (Degruyter & Huber, 2014), evolving magma-mush boundary undergoing phase- and rheological transitions, as suggested by Karlstrom et al. (2012), and more complex injection processes informed by field observations (Poland et al., 2012; Bato et al., 2018, e.g.). Better constraints on the properties of crustal magmatic system from improved geophysical observations (Kiser et al., 2018, e.g.,), and incorporation of more complex features described above, will allow for a more realistic description of the mechanical behaviors of mushy magmatic reservoirs and better interpretations on the observed geodetic and petrologic observations.

Recent studies focusing on the multiphase nature of crustal magmatic systems also shed light on some potentially important physical processes that may be incorporated or combined to our current model. In a recent study by Mittal and Richards (2019), the two-phase nature of the hosting crust of the magma chamber was modeled using similar quantitative methods, with the additional incorporation of a thermal effect (i.e., a thermal-poroviscoelastic description). In this study, gas percolation out of the magma chamber was studied in detail, while the dynamics and deformation of the magma chamber itself was modeled in a simplified fashion (Mittal & Richards, 2019). Future implementation of our current model with a thermal-poroviscoelastic rheology, combined with a crustal-percolation model similar to Mittal and Richards (2019), could extend the one-phase description of the crustal system to a fully two-phase description extending from within the magma chamber to the surface.

In geodynamic models, two-phase systems consisting of melt and rock, such as in mid-ocean-ridges, upper mantle, and subduction zones, have been typically studies using a two-phase fluid models, where compaction of the rock matrix plays an important role in localizing the transport of the lighter, melt phase (McKenzie, 1984; Turcotte & Morgan, 1992; Dymkova & Gerya, 2013; Montési & Zuber, 2002). In the current study, the effect of compaction of the mush matrix is omitted while the mush is considered primarily as a solid phase in resting state with an infinitely large bulk viscosity. It is possible that for a mush layer accumulating in chamber's floor and compacting under crystal settling, a scenario described by McKenzie (2011), could lead to a more prominent effect from compaction and melt segregation. Future studies that relax the radial symmetry condition and incorporate this compaction effect, in combination with chamber deformation, will further extend our understanding on complex mush rheology on the responses of magmatic reservoirs and provide a potential link between magma segregation and ground deformation processes.

5 Summary

In this study, we extend a previous mechanical model by Liao et al. (2018) on mushy magma chambers with poroelastic or viscoelastic mush, by incorporating a more general mush rheology of poroviscoelasticity. We subject the new mushy magma chamber model to an external perturbation of a magma injection with constant injection rate for a duration of time, and observe the similarities and differences caused by different mush rheology on evolution of pressure, stress, magma transport, and surface elevation. We found that the poroviscoelastic mush display both mechanisms of poroviscoelastic diffusion, and viscoelastic relaxation, and that the magma chamber displays features similar to both end members at different stages during its evolution in time. Based on these features, we identify two characteristic timescales that describe the post-injection evolution of the poroviscoelastic mushy chamber: a short-term post-injection time t_{post}^{short} and a long-term post-injection time t_{post}^{long}. Over t_{post}^{short}, the chamber is dominated by poroelastic diffusion characterized by relatively rapid chamber pressure decrease, crustal tensile increase, and transport (i.e.,leaking) of magma from the fluid region to the mush. t_{post}^{long} indicates the period dominated by viscoelastic relaxation, which is characterized by relatively slow decrease in chamber pressure, increase in tensile stress, and inverse transport (i.e., leaking-back) of magma from the mush region to the fluid region. The two characteristic timescales are determined by material properties and geometry of the chamber, but the short-term timescale is more sensitive to the poroelastic diffusion time $\tau_{diffusion}$, and the long-term timescale to the viscoelastic relaxation time $\tau_{relaxation}$. The features of the post-injection evolution of a poroviscoelastic chamber indicate that the poroelastic diffusion mechanism, which causes higher rates of chamber deformation and strain, is more likely to be relevant for potential interpretation of surface observations, while the viscoelastic relaxation, which causes drastic change in the magma transport direc-

378 tion, is potentially relevant for interpreting petrological and geochemical evidence of crys-
379 tal growth.

Acknowledgments

References

386 Abate, J., & Whitt, W.   (2006).   A unified framework for numerically invert-
387   ing laplace transforms.   *INFORMS Journal on Computing*, *18*(4), 408-
388   421.   Retrieved from `https://doi.org/10.1287/ijoc.1050.0137`   doi:
389   10.1287/ijoc.1050.0137

390 Albino, F., Pinel, V., & Sigmundsson, F.   (2010).   Influence of surface load varia-
391   tions on eruption likelihood: application to two icelandic subglacial volcanoes,
392   grímsvötn and katla. *Geophysical journal international*, *181*(3), 1510-1524.

393 Bachmann, O., & Huber, C.   (2016).   Silicic magma reservoirs in the earth's
394   crust.   *American Mineralogist*, *101*(11), 2377–2404.   Retrieved from
395   `http://ammin.geoscienceworld.org/content/101/11/2377`   doi:
396   10.2138/am-2016-5675

397 Bato, M. G., Pinel, V., Yan, Y., Jouanne, F., & Vandemeulebrouck, J.   (2018).
398   Possible deep connection between volcanic systems evidenced by sequen-
399   tial assimilation of geodetic data.   *Scientific Reports*, *8*(1), 11702.   Re-
400   trieved from `https://doi.org/10.1038/s41598-018-29811-x`   doi:
401   10.1038/s41598-018-29811-x

402 Biggs, J., & Pritchard, M. E. (2017). Global volcano monitoring: what does it mean
403   when volcanoes deform? *Elements*, *13*(1), 17-22.

404 Cashman, K. V., Sparks, R. S. J., & Blundy, J. D.   (2017).   Vertically extensive
405   and unstable magmatic systems: A unified view of igneous processes.   *Science*,
406   *355*(6331).   Retrieved from `http://science.sciencemag.org/content/355/`
407   `6331/eaag3055` doi: 10.1126/science.aag3055

408 Cheadle, M., Elliott, M., & McKenzie, D. (2004). Percolation threshold and perme-
409   ability of crystallizing igneous rocks: The importance of textural equilibrium.
410   *Geology*, *32*(9), 757-760.

411 Cheng, A. H.-D. (2016). *Poroelasticity.* Springer International Publishing. doi: doi
412   .org/10.1007/978-3-319-25202-5

413 Currenti, G., & Williams, C. A.   (2014).   Numerical modeling of deformation and
414   stress fields around a magma chamber: Constraints on failure conditions and
415   rheology. *Physics of the Earth and Planetary Interiors*, *226*, 14-27.

416 Degruyter, W., & Huber, C. (2014). A model for eruption frequency of upper crustal
417   silicic magma chambers.   *Earth and Planetary Science Letters*, *403*, 117 - 130.
418   Retrieved from `http://www.sciencedirect.com/science/article/pii/`
419   `S0012821X14004385` doi: https://doi.org/10.1016/j.epsl.2014.06.047

420 Dragoni, M., & Magnanensi, C.   (1989).   Displacement and stress produced by a
421   pressurized, spherical magma chamber, surrounded by a viscoelastic shell.
422   *Physics of the Earth and Planetary Interiors*, *56*(3), 316 - 328. Retrieved from
423   `http://www.sciencedirect.com/science/article/pii/0031920189901660`
424   doi: http://dx.doi.org/10.1016/0031-9201(89)90166-0

425 Dymkova, D., & Gerya, T. (2013). Porous fluid flow enables oceanic subduction ini-
426   tiation on earth. *Geophysical Research Letters*, *40*(21), 5671-5676.

427 Ginibre, C., & Wörner, G.   (2007).   Variable parent magmas and recharge regimes
428   of the parinacota magma system (n. chile) revealed by fe, mg and sr zoning in

429   plagioclase. *Lithos*, *98*(1-4), 118-140.

430 Ginibre, C., Wörner, G., & Kronz, A. (2002). Minor-and trace-element zoning in
431   plagioclase: implications for magma chamber processes at parinacota volcano,
432   northern chile. *Contributions to Mineralogy and Petrology*, *143*(3), 300-315.

433 Grosfils, E. B. (2007). Magma reservoir failure on the terrestrial planets: Assess-
434   ing the importance of gravitational loading in simple elastic models. *Journal of*
435   *Volcanology and Geothermal Research*, *166*(2).

436 Gudmundsson, A. (2012). Magma chambers: Formation, local stresses, ex-
437   cess pressures, and compartments. *Journal of Volcanology and Geother-*
438   *mal Research*, *237-238*(Supplement C), 19 - 41. Retrieved from `http://`
439   `www.sciencedirect.com/science/article/pii/S0377027312001539` doi:
440   https://doi.org/10.1016/j.jvolgeores.2012.05.015

441 Humphreys, M. C., Blundy, J. D., & Sparks, R. S. J. (2006). Magma evolution and
442   open-system processes at shiveluch volcano: Insights from phenocryst zoning.
443   *Journal of Petrology*, *47*(12), 2303-2334.

444 Huppert, H. E., & Woods, A. W. (2002, 12 05). The role of volatiles in magma
445   chamber dynamics. *Nature*, *420*(6915), 493–495. Retrieved from `http://dx`
446   `.doi.org/10.1038/nature01211`

447 Jellinek, A. M., & DePaolo, D. J. (2003, Jul 01). A model for the origin of large sili-
448   cic magma chambers: precursors of caldera-forming eruptions. *Bulletin of Vol-*
449   *canology*, *65*(5), 363–381. Retrieved from `https://doi.org/10.1007/s00445`
450   `-003-0277-y` doi: 10.1007/s00445-003-0277-y

451 Karlstrom, L., Dufek, J., & Manga, M. (2010). Magma chamber stability in arc
452   and continental crust. *Journal of Volcanology and Geothermal Research*,
453   *190*(3), 249 - 270. Retrieved from `http://www.sciencedirect.com/`
454   `science/article/pii/S0377027309003977` doi: https://doi.org/10.1016/
455   j.jvolgeores.2009.10.003

456 Karlstrom, L., Rudolph, M. L., & Manga, M. (2012). Caldera size modulated by
457   the yield stress within a crystal-rich magma reservoir. *Nature Geoscience*,
458   *5*(6), 402–405. Retrieved from `https://doi.org/10.1038/ngeo1453` doi:
459   10.1038/ngeo1453

460 Kiser, E., Levander, A., Zelt, C., Schmandt, B., & Hansen, S. (2018). Focusing
461   of melt near the top of the mount st. helens (usa) magma reservoir and its
462   relationship to major volcanic eruptions. *Geology*, *46*(9), 775-778.

463 Le Mével, H., Feigl, K. L., Córdova, L., DeMets, C., & Lundgren, P. (2015). Evo-
464   lution of unrest at laguna del maule volcanic field (chile) from insar and gps
465   measurements, 2003 to 2014. *Geophysical Research Letters*, *42*(16), 6590-
466   6598. Retrieved from `https://agupubs.onlinelibrary.wiley.com/doi/abs/`
467   `10.1002/2015GL064665` doi: 10.1002/2015GL064665

468 Le Mével, H., Gregg, P. M., & Feigl, K. L. (2016, 08). Magma injection into a
469   longlived reservoir to explain geodetically measured uplift: Application to the
470   2007–2014 unrest episode at laguna del maule volcanic field, chile. *Jour-*
471   *nal of Geophysical Research. Solid Earth*, *121*(8), 6092–6108. Retrieved
472   from `http://www.ncbi.nlm.nih.gov/pmc/articles/PMC5101856/` doi:
473   10.1002/2016JB013066

474 Liao, Y., Soule, S. A., & Jones, M. (2018, 2019/03/11). On the mechanical effects of
475   poroelastic crystal mush in classical magma chamber models. *Journal of Geo-*
476   *physical Research: Solid Earth*, *123*(11), 9376–9406. Retrieved from `https://`
477   `doi.org/10.1029/2018JB015985` doi: 10.1029/2018JB015985

478 Magee, C., Stevenson, C. T., Ebmeier, S. K., Keir, D., Hammond, J. O., Gottsmann,
479   J. H., . . . Petronis, M. S. (2018). Magma plumbing systems: a geophysical
480   perspective. *Journal of Petrology*, *59*(6), 1217-1251.

481 McKenzie, D. (1984). The generation and compaction of partially molten rock.
482   *Journal of petrology*, *25*(3), 713-765.

483 McKenzie, D. (2011, 05). Compaction and crystallization in magma chambers: To-

wards a model of the skaergaard intrusion. *Journal of Petrology*, *52*(5), 905–930. Retrieved from `http://dx.doi.org/10.1093/petrology/egr009`

McTigue, D. F. (1987). Elastic stress and deformation near a finite spherical magma body: Resolution of the point source paradox. *Journal of Geophysical Research: Solid Earth*, *92*(B12), 12931–12940. Retrieved from `http://dx.doi.org/10.1029/JB092iB12p12931` doi: 10.1029/JB092iB12p12931

Mittal, T., & Richards, M. A. (2019). Volatile degassing from magma chambers as a control on volcanic eruptions. *Journal of Geophysical Research: Solid Earth*, *124*(8), 7869-7901. Retrieved from `https://agupubs.onlinelibrary.wiley.com/doi/abs/10.1029/2018JB016983` doi: 10.1029/2018JB016983

Montési, L. G., & Zuber, M. T. (2002). A unified description of localization for application to largescale tectonics. *Journal of Geophysical Research: Solid Earth*, *107*(B3), 1-21.

Parmigiani, A., Huber, C., & Bachmann, O. (2014). Mush microphysics and the reactivation of crystalrich magma reservoirs. *Journal of Geophysical Research: Solid Earth*, *119*(8), 6308-6322.

Perugini, D., Poli, G., & Valentini, L. (2005, Jun 01). Strange attractors in plagioclase oscillatory zoning: petrological implications. *Contributions to Mineralogy and Petrology*, *149*(4), 482–497. Retrieved from `https://doi.org/10.1007/s00410-005-0667-6` doi: 10.1007/s00410-005-0667-6

Pinel, V., & Jaupart, C. (2003). Magma chamber behavior beneath a volcanic edifice. *Journal of Geophysical Research: Solid Earth*, *108*.

Poland, M. P., Miklius, A., Sutton, A. J., & Thornber, C. R. (2012). A mantle-driven surge in magma supply to kīlauea volcano during 2003–2007. *Nature Geoscience*, *5*(4), 295-300.

Ruprecht, P., & Wörner, G. (2007). Variable regimes in magma systems documented in plagioclase zoning patterns: El misti stratovolcano and andahua monogenetic cones. *Journal of Volcanology and Geothermal Research*, *165*(3-4), 142-162.

Segall, P. (2016). Repressurization following eruption from a magma chamber with a viscoelastic aureole. *Journal of Geophysical Research: Solid Earth*, *121*(12), 8501–8522. Retrieved from `http://dx.doi.org/10.1002/2016JB013597` (2016JB013597) doi: 10.1002/2016JB013597

Segall, P. (2019). Magma chambers: what we can, and cannot, learn from volcano geodesy. *Philosophical Transactions of the Royal Society A: Mathematical, Physical and Engineering Sciences*, *377*(2139), 20180158. Retrieved from `https://royalsocietypublishing.org/doi/abs/10.1098/rsta.2018.0158` doi: 10.1098/rsta.2018.0158

Singer, B. S., Le Mével, H., Licciardi, J. M., Córdova, L., Tikoff, B., Garibaldi, N., ... Feigl, K. L. (2018). Geomorphic expression of rapid holocene silicic magma reservoir growth beneath laguna del maule, chile. *Science Advances*, *4*(6). Retrieved from `http://advances.sciencemag.org/content/4/6/eaat1513` doi: 10.1126/sciadv.aat1513

Sparks, R. S. J., & Cashman, K. V. (2017). Dynamic magma systems: Implications for forecasting volcanic activity. *Elements*, *13*(1), 35–40. Retrieved from `http://elements.geoscienceworld.org/content/13/1/35` doi: 10.2113/gselements.13.1.35

Turcotte, D. L., & Morgan, J. P. (1992). The physics of magma migration and mantle flow beneath a midocean ridge. *Mantle Flow and Melt Generation at MidOcean Ridges*, *71*, 155-182.

Ward, K. M., Zandt, G., Beck, S. L., Christensen, D. H., & McFarlin, H. (2014). Seismic imaging of the magmatic underpinnings beneath the altiplano-puna volcanic complex from the joint inversion of surface wave dispersion and receiver functions. *Earth and Planetary Science Letters*, *404*, 43-53.

Zhan, Y., & Gregg, P. (2019). How accurately can we model magma reservoir fail-

539   ure with uncertainties in host rock rheology?   *Journal of Geophysical Research:*
540   *Solid Earth*.

541   ## Appendix A   Governing equations and solution method

The quantitative treatment of the equations of motions and boundary conditions follows closely (Liao et al., 2018). Specifically, we could obtain the poroviscoelastic solutions by transforming the poroelastic solutions in (Liao et al., 2018) under correspondence principle. The poroviscoelastic rheology can be alternatively expressed using Laplace transform

$$\widetilde{\boldsymbol{\sigma}_m} = (K_m - \frac{2}{3}\overline{\mu_m})\nabla \cdot \widetilde{\vec{u}_m}\boldsymbol{I} + \overline{\mu_m}\left(\nabla\widetilde{\vec{u}_m} + \nabla\widetilde{\vec{u}_m}^T\right) - \alpha\widetilde{P_f}\boldsymbol{I} \tag{A1a}$$

$$\widetilde{m} = \rho_f\alpha(\nabla \cdot \widetilde{\vec{u}_m} + \frac{\alpha}{K_u - K_m}\widetilde{P_f}) \tag{A1b}$$

where the Laplace transform is defined as $\widetilde{f(r,s)} \equiv \int_0^\infty f(r,t)e^{-st}\mathrm{dt}$. The effect of viscous relaxation is reflected by a rigidity that varies with time (i.e., function of s under Laplace transform)

$$\overline{\mu_m} = \mu_m\frac{\eta_m s}{\eta_m s + \mu_m}$$

From the equilibrium condition $\nabla \cdot \widetilde{\boldsymbol{\sigma}} = 0 \rightarrow \nabla\left((K_m + \frac{4}{3}\overline{\mu_m})\nabla \cdot \widetilde{\vec{u}} - \alpha\widetilde{P_f}\right) = 0$, we can define time-dependent function $\zeta(t)$ such that its Laplace transform

$$\widetilde{\zeta}(s) = (K_m + \frac{4}{3}\overline{\mu_m})\nabla \cdot \widetilde{\vec{u}} - \alpha\widetilde{P_f}$$

Following steps in (Liao et al., 2018) and non-dimensionelize the system by length scale R_o (chamber radius), time scale η_m/μ_m (relaxation time) and stress/pressure scale μ_r (rock rigidity), the boundary values have the relation

$$\widetilde{P_f}\left(\frac{r_o}{R_o}\right) = \overline{a_1}\widetilde{m}\left(\frac{r_o}{R_o}\right) + \overline{a_2}\widetilde{\zeta} \tag{A2a}$$

$$\widetilde{u_m}\left(\frac{r_o}{R_o}\right) = \overline{b_1}\int_{\frac{r_o}{R_o}}^1 r'^2\widetilde{m}(r')\mathrm{d}r' + \overline{b_2}\widetilde{\zeta} + \widetilde{u_m}(1)\frac{R_o^2}{r_o^2} \tag{A2b}$$

$$\widetilde{\sigma_m^{rr}}\left(\frac{r_o}{R_o}\right) = \overline{c_1}\int_{\frac{r_o}{R_o}}^1 r'^2\widetilde{m}(r')\mathrm{d}r' + \overline{c_2}\widetilde{\zeta} + \overline{c_3}\widetilde{u_m}(1) \tag{A2c}$$

$$\widetilde{\sigma_m^{rr}}(1) = \widetilde{\zeta} - 4\frac{\overline{\mu_m}}{\mu_r}\widetilde{u_m}(1) \tag{A2d}$$

$$\widetilde{P_l} = \overline{d_1}\int_{\frac{r_o}{R_o}}^1 r^2\widetilde{m}(r)\mathrm{d}r + \overline{d_2}\widetilde{\zeta} - \frac{3K_l R_o^3}{\mu_r r_o^3}\widetilde{u_m}(1) + \overline{f_4} \tag{A2e}$$

where $\overline{f_4} = \frac{K_l}{\mu_r}\frac{\Delta M}{M_o}\frac{1}{s}$ (for instantaneous injection) or $\overline{f_4} = \frac{K_l}{\mu_r}\frac{\Delta M}{M_o}\frac{1-e^{st_{inj}}}{s^2 t_{inj}}$ (for gradual injection), and the s-dependent coefficients $\overline{a_1}, \overline{a_2}, \overline{b_1}, \overline{b_2}, \overline{c_1}, \overline{c_2}, \overline{d_1}, \overline{d_2}$ have the same forms as those defined in Appendix A.2.4 in (Liao et al., 2018) while substituting $\overline{\mu}(s)$ for mush rigidity. Substituting (A2) into the boundary conditions and into Darcy's law, mass conservation, and equilibrium condition, we obtain (dimensionless) constraint on the fluid content $\widetilde{m}$

$$\nabla^2\widetilde{m} - \frac{\tau_{diffusion}}{\tau_{relaxation}}\frac{s(s + \frac{K_u}{K_u + \frac{4}{3}\mu_m^o})}{(s + \frac{K_m}{K_m + \frac{4}{3}\mu_m^o})}\widetilde{m} = 0 \tag{A3}$$

and the boundary conditions

$$\frac{\partial\widetilde{m}}{\partial r}(r = 1) = 0, \qquad \widetilde{a_1}\widetilde{m}(\frac{r_o}{R_o}) + \overline{h_o}\int\widetilde{m}r^2 dr = \overline{h1}$$

where $\overline{h_0}$ and $\overline{h_1}$ have the same form of h_0 and h_1 in §A.2.4 in (Liao et al., 2018) with $\mu_m \to \overline{\mu_m}$. Solving (A3) with the boundary conditions and using the relations between m, $\vec{u}$ and P_f similar to those in (Liao et al., 2018), we can find the solutions for $\widetilde{m}$

$$\widetilde{m} = \frac{Ae^{r\sqrt{S_o}}}{\sqrt{S_o}r} + \frac{Be^{-r\sqrt{S_o}}}{\sqrt{S_o}r} \tag{A4}$$

with

$$S_o = \frac{\tau_{diffusion}}{\tau_{relaxation}} \frac{s(s + \frac{K_u}{K_u + \frac{4}{3}\mu_m^o})}{(s + \frac{K_m}{K_m + \frac{4}{3}\mu_m^o})}, \qquad A = \frac{\widetilde{h_1}S_o^{\frac{3}{2}}(\sqrt{S_o}+1)e^{-\sqrt{S_o}}}{2\overline{g}}, \qquad B = \frac{\widetilde{h_1}S_o^{\frac{3}{2}}(\sqrt{S_o}-1)e^{\sqrt{S_o}}}{2\overline{g}}$$

$$\overline{g} = \sqrt{S_o}\left(\frac{\overline{a_1}R_o}{r_o}S_o + \overline{h_0}\left(1 - \frac{r_o}{R_o}\right)\right)\cosh\left(\sqrt{S_o}\left(1 - \frac{r_o}{R_o}\right)\right) + \left(\left(\overline{h_0}\frac{r_o}{R_o} - \frac{\overline{a_1}R_o}{r_o}\right)S_o - \overline{h_0}\right)\sinh\left(\sqrt{S_o}\left(1 - \frac{r_o}{R_o}\right)\right)$$

The Laplace transform of other quantities can all be obtained via (A4), such as core pressure, rock tensile stress and radial stress at the chamber's wall

$$\widetilde{\sigma_{rock}^{\theta\theta}}(1) = -2\frac{\overline{f_4}}{\overline{g_2}} - 2\frac{\overline{g_1}}{\overline{g_2}}\int_{\frac{r_o}{R_o}}^{1}\widetilde{m}r^2 dr$$

$$\widetilde{\sigma_m^{rr}}(1) = \widetilde{\sigma_{rock}^{rr}}(1) = -2\widetilde{\sigma_{rock}^{\theta\theta}}(1) \tag{A5}$$

$$\widetilde{\zeta} = 2\left(4\frac{\overline{\mu_m}}{\mu_r} - 1\right)\widetilde{\sigma^{\theta\theta}}$$

$$\widetilde{P_l} = \overline{a_1}\widetilde{m}\left(\frac{r_o}{R_o}\right) + \overline{a_2}\widetilde{\zeta}$$

Following (McTigue, 1987), we apply a first order correction to obtain surface deformation. The pressure-stress coupling in (McTigue, 1987) is here replaced by a stress-stress coupling at the chamber-crust interface, and the radial component of poroviscoelastic stress plays the role of a virtual pressure in the chamber, leading to the surface deformation (McTigue, 1987; Segall, 2016)
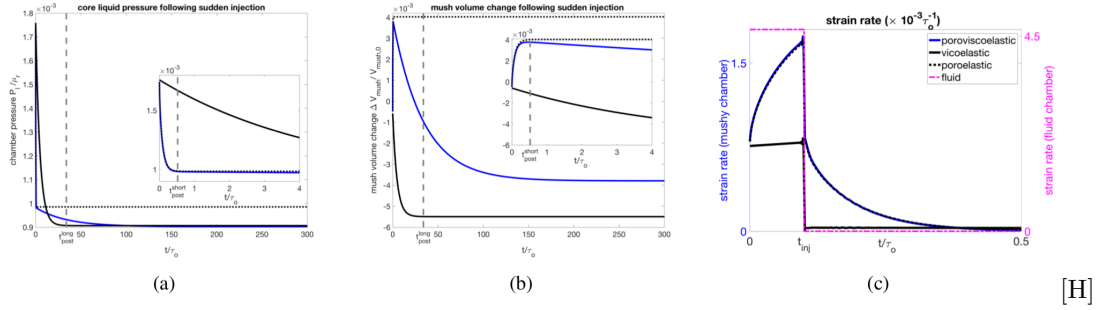
$$\widetilde{u_z}(\rho, 0) = -\widetilde{\sigma_m^{rr}}(1)\frac{d}{R_0}\left(\frac{R_0}{d}\right)^3\frac{1-\nu}{\left(\frac{\rho^2}{d^2}+1\right)^{\frac{3}{2}}}$$

$$\widetilde{u_\rho}(\rho, 0) = -\widetilde{\sigma_m^{rr}}(1)\frac{\rho}{R_0}\left(\frac{R_0}{d}\right)^3\frac{1-\nu}{\left(\frac{\rho^2}{d^2}+1\right)^{\frac{3}{2}}} \tag{A6}$$

where u_z and u_ρ are vertical and horizontal displacement on the surface (normalized by chamber radius R_0) measured at distance ρ from the center of the chamber's projection, ν is Poisson's ratio of the elastic crust. We numerically invert the Laplace solutions to obtain solutions using a matlab code shared on Mathworks File Exchange, which is based on the scheme proposed in (Abate & Whitt, 2006). The Laplace solution allows us to define the longest timescale in the system. Similar to (Liao et al., 2018), the Laplace solutions can be inverted using the Mellin inversion formula, which yields the solutions in real space as a superposition of exponentially decaying terms in the form of
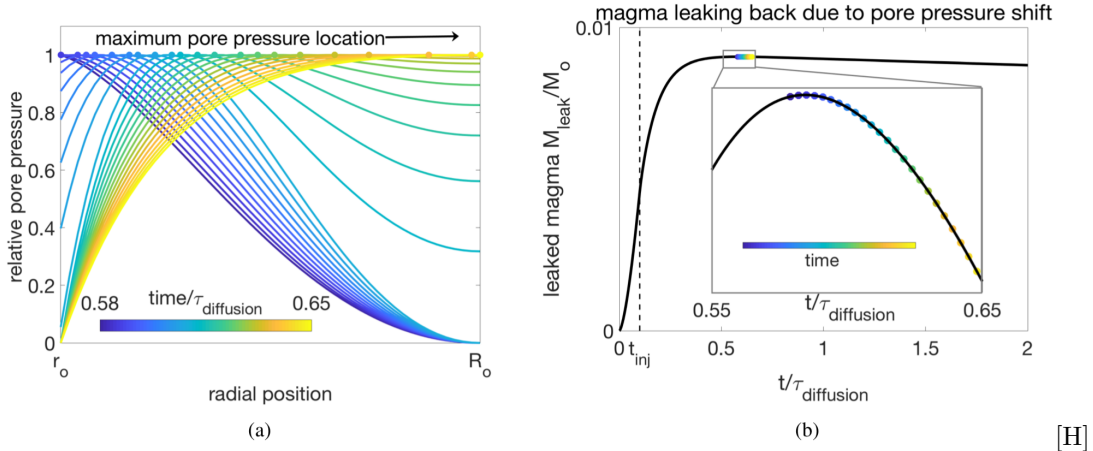
$$A(r,t) = A_0(r) + A_1(r)e^{-t/\tau_1} + A_2(r)e^{-t/\tau_2} + ...$$

where τ_1 is the largest decay period, and can be solved graphically given the parameters of the system. We use this timescale to determine the longest timescale in the system's post-injection evolution t_{post}^{long} (Liao et al., 2018).
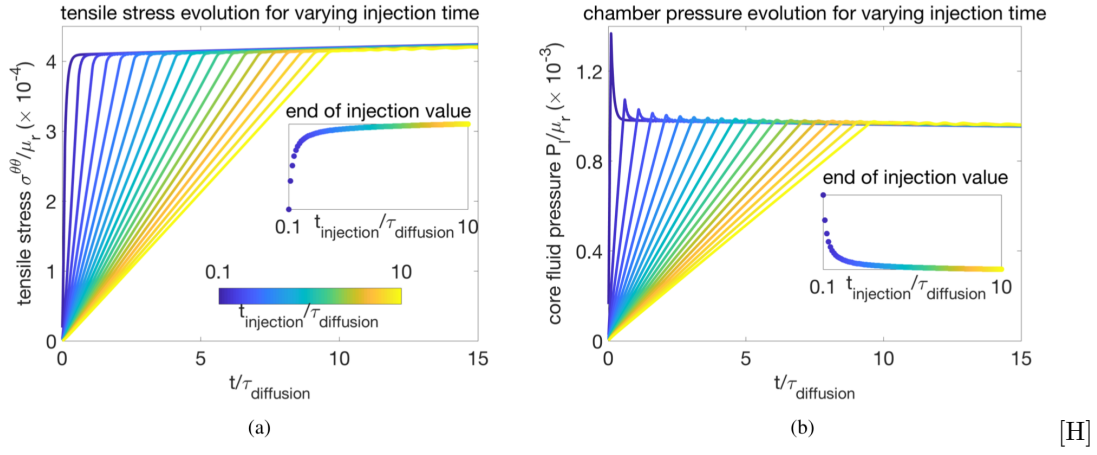
Appendix B Additional model results

(a)   (b)   (c)   [H]

Figure B1. Panel (a) and (b): post-injection short-term and long-term evolution for core pressure and mushy deformation for three cases (poroviscoelastic, poroelastic, and viscoelastic). Inset panels are zoom-in of the beginning period of the evolution, and grey broken lines indicate the two post-injection timescales t_{post}^{long} and t_{post}^{short}. Panel (c): tensile strain rate $\dot{\epsilon}^{\theta\theta} = \dot{u}(R_o)/R_o$ at the wall of the chamber during and after the injection, for four different cases. For mushy chamber, the strain rate is highest at the end of the injection, and remains positive during short-term post-injection evolution. During long-term post-injection evolution, the strain rate becomes indiscernible.

(a)   (b)   [H]

Figure B2. Panel (a) cumulative amount of leaked magma M_{leak} as a function of time during and after the injection. Panel (b) shows the the relative pore pressure $\frac{P_f - min(P_f)}{max(P_f) - min(P_f)}$ as function of radial position in the mush shell. Colored lines in (b) correspond to colored data points in (a). The decrease in M_{leak} with time corresponds to the shift of maximum pore pressure from the inner boundary of the much outwards.

Figure B3.   Evolution of core pressure and tensile stress with time for varying injection time length t_{inj}. The system has $\tau_{diffusion} = \tau_{relaxation}$. Insets show the values at the end of the injection. As t_{inj} increases, the short-term evolution period shortens and become less apparent.